ACS OMEGA

http://pubs.acs.org/journal/acsodf

Article

# Study of Two-Dimensional Janus WXY (X≠Y= S, Se, and Te) Trilayer Homostructures for Photovoltaic Applications Using DFT Screening of Different Stacking Patterns

Khadijatul Kubra, Md. Rafiqul Islam, Md. Sakib Hasan Khan, Muhammad Shaffatul Islam, and Md. Tanvir Hasan*

Cite This: *ACS Omega* 2022, 7, 12947−12955

Read Online

ACCESS | Metrics & More | Article Recommendations | Supporting Information

**ABSTRACT:** Based on the first-principles density functional theory, Janus WXY (X ≠ Y = S, Se, and Te) trilayer homostructures for different stacking patterns are studied in this work to analyze their appropriateness in fabricating photovoltaic (PV) devices. A total of fifteen trilayer homostructures are proposed, corresponding to the suitable five stacking patterns, such as AAA, AA′A, ABA, AB′A, and A′BA′ for each Janus WXY (X ≠ Y = S, Se, and Te) material. Structural and energetic parameters for all the fifteen structures are evaluated and compared to find energetically stable structures, and dynamic stability is confirmed by phonon dispersion curves. All these configurations being homostructure, lattice mismatch is found to be very low (∼0.05%), unlike heterostructure, making them feasible for optoelectronics and PV applications. WSSe AAA, WSSe AA′A, and WSeTe AA′A are dynamically stable along with negative binding energy and show type-II band alignment, enabling effective spatial carrier separation of photogenerated carriers. The optical properties of dynamically stable WSSe AAA and WSSe AA′A structures are also calculated, and the absorption coefficients at the visible light region are found to be ∼3.5 × $10^5$ $cm^{-1}$, which is comparable to the perovskite material absorption coefficient. Moreover, we have compared the optical characteristics of dynamically stable WSSe AAA and WSSe AA′A structures with their monolayer structures to realize the significance of stacking trilayer structures. Electrical properties such as mobility and conductivity for dynamically stable WSSe AAA and WSSe AA′A structures are evaluated to suggest them as a probable efficient material in PV technology.

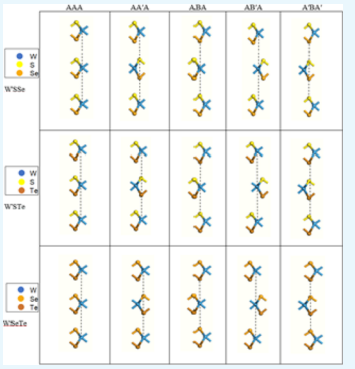


## 1. INTRODUCTION

The necessity of energy has increased tremendously over time. Unlike fossil fuels, solar energy will not run out, and it has minimal pollution or physical danger compared to fossil fuels. For the large-scale commercialization of solar energy, cost-effective photovoltaic (PV) technology is needed that produces high-efficiency solar cells. Thin-film solar cells could be a promising solution for this target by offering low processing and material costs.[1] For the construction of ultrathin PV cells, two-dimensional (2D) materials have advantages over traditional materials in having properties such as a desirable band gap value, high conductivity, high crystalline quality, strong light−matter interaction, high thermal stability, and extraordinary flexibility.[2,3] Study on the applications of ultrathin PV devices based on 2D transition metal dichalcogenides (TMDs) and their offshoots have been continuing.[4−8] Even though light−matter interactions in TMDs are very strong, TMD-based PV devices have low power conversion efficiency, usually less than one percent because of their inefficient light absorption, limiting their practical applications.[9]

Recently, a new type of TMD, Janus monolayer (ML) MoSSe, where the chalcogenides S and Se atoms are covalently bonded with metal Mo atoms, was successfully synthesized experimentally using the chemical vapor deposition method by the sulfurization of ML MoSe2.[10] Correspondingly, Janus WSSe ML was synthesized using pulsed laser ablation plasmas by implanting Se species into the WS2 ML.[11] Similar Janus TMDs (JTMDs), where the metal layer has different atomic species on each side, have been documented to exhibit applicable band gaps and, within the ultraviolet to visible light regions, show strong optical absorption by using a first-principles study.[12,13] Because of the presence of strong planar asymmetry in JTMDs, the difference in electronegativity of chalcogens causes the formation of a dipole across the plane, which induces an internal electric field.[14−16] When stacking multiple JTMD layers, the dipoles of the individual layers are stacked and an abrupt thin pn junction can be obtained across the multilayer system; this way, JTMDs can be integrated

Received: January 12, 2022
Accepted: March 24, 2022
Published: April 7, 2022

effectively for optoelectronic and PV devices.[17−19] For example, Palsgaard et al.[20] have demonstrated that three layers of stacked MoSSe Janus structures having type-II band alignment can result in abrupt inherently atomically thin p−n junctions across the layers, and using such a multilayer stacked device, the photocurrent response is higher than that of an analogous thin-film silicon device, explaining the great prospective of stacked Janus in PV technology. Several pieces of studies have been carried out till now to investigate the electrical, mechanical, transport, and optical properties of ML and bilayer Janus MXY (M = W/Mo; X ≠ Y = S, Se, and Te),[21−24] where all the structures show planar asymmetry resulting in strong dipoles across the plan, indicating their appropriateness in PV applications.

However, detailed analysis of the electronic and optical properties of trilayer homostrctures of Janus WXY (X ≠ Y = S, Se, and Te) for different vertical stacking patterns has not been studied yet for PV applications. Therefore, in this study, comparative studies were performed to validate the stability of possible fifteen homostructures for five stacking patterns of Janus WXY (X ≠ Y = S, Se, and Te) trilayers. The dynamically stable structures among these fifteen structures are chosen for a detailed study on their electronic and optical properties to examine their significance in PVs. These studies suggest that different stacking patterns can be considered as appropriate candidate materials for PV technology.

**2. Computational Methodology.** First-principles density functional theory (DFT) calculations are conducted using the Cambridge Serial Total Energy Package (CASTEP) by utilizing a plane-wave basis set.[25,26] All the geometry optimizations are performed using generalized gradient approximation (GGA) according to the Perdew−Buerke−Enrnzerhof (PBE) functionals as an exchange−correlation potential[27] and by following the Broyden−Fletcher−Goldfarb−Shanno algorithm as the numerical iterative method with a cutoff energy of 600 eV and energy relaxation of $1 \times 10^{-5}$ eV/atom. For dynamical stability prediction, phonon dispersion curves are introduced by DFT calculation with local density approximation (LDA) as a local exchange−correlation functional based on the Ceperley and Alder data parameterized by Perdew and Zunger (PZ) in the CASTEP.[28] For convergence, the stress error tolerance, Hellmann−Feynman force, and displacement tolerance cutoff are 0.05 GPa, 0.03 eV/Å, and 0.001 Å, respectively. The self-consistent field method used has fine convergence thresholds of $1 \times 10^{-6}$ eV/atom and electron−ion interactions are defined by the norm-conserving pseudopotential incorporating the Koelling−Harmon relativistic effect.[29] At first, electronic properties are described using the GGA-PBE functional. Conventionally, for homostructured semiconducting materials, band gap calculation using the GGA-PBE functional gives an underestimated value of the experimental band gap. Therefore, nonlocal hybrid functional Heyd−Scusena−Ernzerhof's (HSE06)[30] is used for band gap prediction. On the other hand, the LDA functional considers only edge density, so this functional underestimates band gap values. Therefore, to calculate the band edge position and band offset, LDA-PZ with a double zeta basis set is considered. A vacuum space of 40 Å in the $z$-direction is considered throughout the calculations to avoid interaction between adjacent layers. The effect of van der Waals (vdW) interaction between the stacking layers of homostructures is considered through the DFT-D2 method based on the Grimme scheme.[31] The Brillouin zones are sampled with 9 × 9 × 1 and 15 × 15 × 1 $k$-points for electronic and optical property computations, respectively.

The mobility of the carriers is attained by using the semi-classical Boltzmann transport equation (BTE)[32] as given by

$$\mu = -2q\frac{\sum_{kn} v_{kn}^2 \frac{\partial f_{kn}^0}{\partial \epsilon_{kn}} \tau_{kn}}{\sum_{kn} f_{kn}^0} \tag{1}$$

Here, $k$, $n$, q, $\epsilon_{kn}$, $v_{kn}$, and $\tau_{kn}$ are electron momentum, band index, charge, electron velocity, energy, and relaxation time, respectively. The electronic distribution of the particles f is defined by the BTE

$$\frac{qE}{\hbar}\cdot\Delta_k f_{kn} = \left(\frac{\partial f_{kn}}{\partial t}\right)_{\text{Coll}} = \frac{\delta f}{\tau_{kn}} \tag{2}$$

Expression of the inverse relaxation time[32]

$$\frac{1}{\tau_{kn}} = \sum_{k'n'}\left(1 - \frac{\delta f_{k'n'}}{\delta f_{kn}}\right)P_{kk'}^{nn'} \tag{3}$$

Here, $P_{kk'}^{nn'}$ is the transition rate from state $kn$ to $k'n'$.

For each configuration, relaxation time is obtained according to eq 3 based on Fermi's golden rule by calculating the electron−phonon coupling matrix from dynamical matrix and Hamiltonian matrix on a fine grid of $k$-points and $n$-points in the Quantum ESPRESSO[33] platform by solving DFT self-consistently. Finally, to calculate mobility, the BTE by the relaxation time approximation is estimated in this software package by carrying out ground state calculation using the LDA-PZ functional.

Dielectric function $\varepsilon(\omega) = \varepsilon_1(\omega)+i\varepsilon_2(\omega)$ based on DFT, where $\varepsilon_1(\omega)$ and $\varepsilon_2(\omega)$ are real and imaginary parts, respectively, are evaluated by[34]

$$\varepsilon_2 = \frac{2e^2\pi}{\Omega\,\varepsilon_0}\sum_{k,v,c}|\langle\Psi_k^c|\hat{u}\times r|\Psi_k^v\rangle|^2\delta(E_k^c - E_k^v - E) \tag{4}$$

Here, Ω = polarization density, $e$ = electronic charge, $r$ = spatial position, $\hat{u}$ = polarization of incident filed, $\Psi_k^c$ and $\Psi_k^v$ = the conduction band (CB) and valence band (VB) wave function at $k$, respectively, $E$ = Fermi energy, $E_k^v$ = VB energy, and $E_k^c$ = CB energy.

The optical absorption coefficient is computed from the dielectric function by the following formula[35]

$$\alpha(\omega) = \sqrt{2}\,\omega\sqrt{\left[\sqrt{\varepsilon_1^2(\omega) + \varepsilon_2^2(\omega)} - \varepsilon_1(\omega)\right]} \tag{5}$$

## 3. RESULTS AND DISCUSSION

**3.1. Structural Properties.** In Janus WXY (X ≠ Y = S, Se, and Te), the electronegativity difference between X and Y chalcogenide atoms results in an in-built cross-plan (cp) dipole. The reason can be realized from the amount of transferred charge from the W atom to the X and Y atoms due to the difference in electronegativity by the analysis of Bader charge transfer.

Table 1 shows Bader charges for Janus WXY MLs; here, differences in charge transfer suggest unequal charge distribution, which creates an intrinsic electric field, unlike TMDs. At first, MLs of Janus WXY (X ≠ Y = S, Se, and Te) are vertically stacked to form trilayer homostructures with the


https://doi.org/10.1021/acsomega.2c00244
ACS Omega 2022, 7, 12947−12955

**Table 1. Bader Charges ΔQ for Janus WXY MLs Where Positive and Negative Values Represent the Charge Depletion and Accumulation, Respectively**

| WXY (X ≠ Y = S, Se, Te) | $\Delta Q_w$ (e) | $\Delta Q_x$ (e) | $\Delta Q_y$ (e) |
|---|---|---|---|
| WSSe | 1.088 | −0.607 | −0.481 |
| WSTe | 0.801 | −0.628 | −0.174 |
| WSeTe | 0.564 | −0.443 | −0.121 |

five most usual stacking patterns, AAA, AA′A, ABA, AB′A, and A′BA′, constituting a total of fifteen configurations for our study, which is shown in Figure 1.

While stacking, lattice mismatches of the configurations were found to be very low (∼0.05%) because of the homostructure. For each configuration in Figure 1, the top layer has a higher electronegativity material facing vacuum, and the bottom layer has a lower electronegativity material facing vacuum. Lattice constants of the geometrically optimized structures of fifteen configurations were found to be very much compatible with their ML structures (3.274 Å for Mono WSSe, 3.387 Å for Mono WSTe, and 3.471 Å for Mono WSeTe) and also have minimal differences among the different stacking patterns of the same material as listed in Table S1a−c.

As for the determination of dynamical stability, phonon dispersion analysis is done using DFT calculation. Among all the fifteen configurations. Structures WSSe AAA, WSSe AA′A, and WSeTe AA′A are dynamically stable, not having any negative phonon branches, and comparable to the dynamically stable Mono WSSe and Mono WSeTe phonon dispersion curves, as shown in Figure 2a−e. The rest of the twelve structures are not dynamically stable because they have negative phonon frequencies in the phonon dispersion curves as per Figure S7. Hence, for our further study, we will be focused mainly on WSSe AAA, WSSe AA′A, and WSeTe AA′A configurations. The sum of vdW and covalent radii of the stacking atoms are calculated to comment on the possibility of the existence of a covalent bond. The smallest cross-layer spacing in WSSe AAA (WSSe AA′A and WSeTe AA′A) between the top layer and the middle layer is 3.81 Å (3.16 and 3.44 Å) and between the bottom layer and middle layer is 3.81 Å (3.18 and 3.44 Å), which is higher than the sum of the covalent radii of S 1.02 Å (S 1.02 and Se 1.16 Å) and Se 1.16 Å (Se 1.16 and Te 1.35 Å) atoms, that is, 2.18 Å (2.18 and 2.51 Å), signifying the nonappearance of covalent bonding between the adjacent layers. To evaluate the energetical stability at the ground state of dynamically stable structures WSSe AAA, WSSe AA′A, and WSeTe AA′A and compare them with the rest of the twelve structures, the binding energy of each structure is calculated as

$$E_b = E_{WXY-trilayer} - 3 \times E_{WXY-monolayer} \quad (6)$$

Here, $E_{WXY\text{-}trilayer}$ and $E_{WXY\text{-}monolayer}$, respectively, are the total energies of the geometry-optimized WXY trilayer and WXY

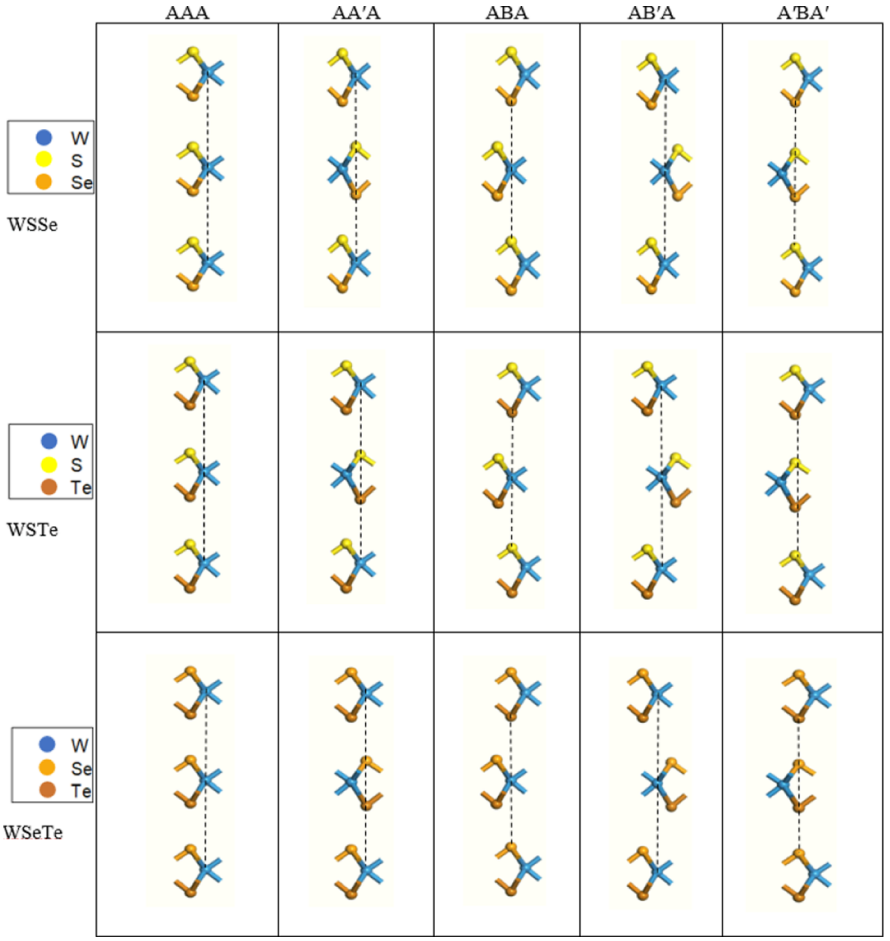


**Figure 1.** Side views of the atomic configurations of WSSe, WSTe, and WSeTe trilayer homostructures. W, S, Se, and Te atoms are denoted by blue, yellow, orange, and bronze spheres, respectively.



https://doi.org/10.1021/acsomega.2c00244
ACS Omega 2022, 7, 12947−12955

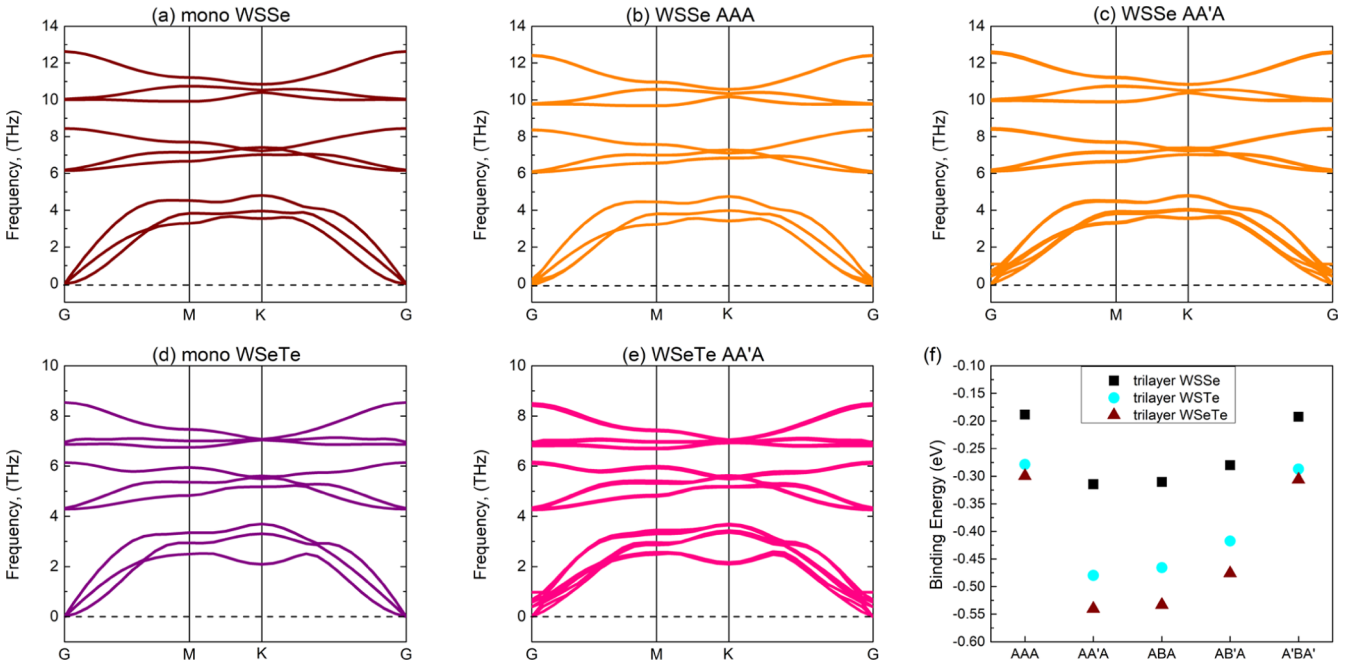


**Figure 2.** Phonon dispersion curves for (a) Mono WSSe, (b) WSSe AAA, (c) WSSe AA′A, (d) Mono WSeTe, (e) WSeTe AA′A, and (f) binding energies of the equilibrium geometric configurations of WSSe, WTeS, and WTeSe trilayer.

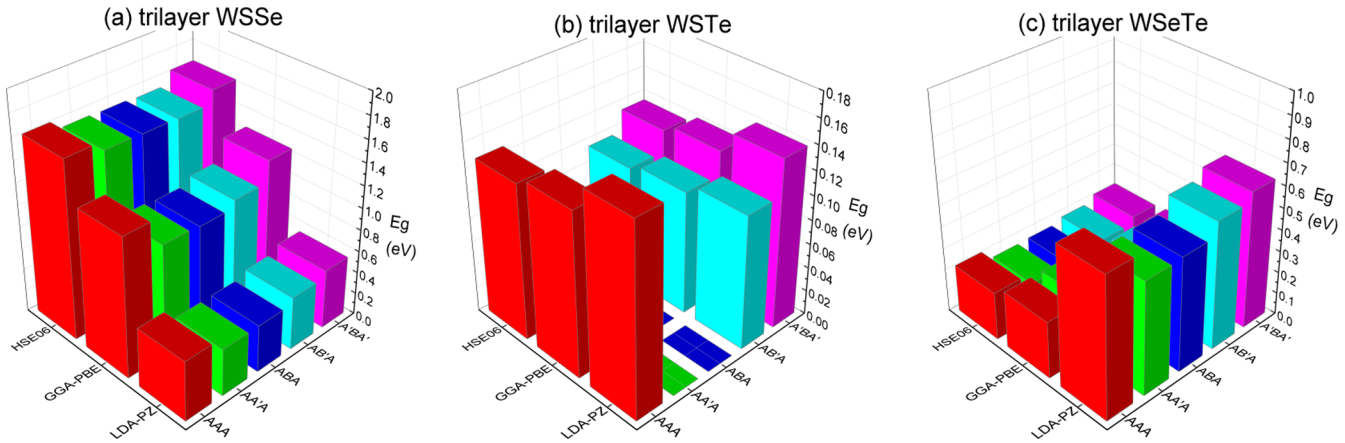


**Figure 3.** Comparison of band gaps of (a) WSSe, (b) WSTe, and (c) WSeTe trilayer of different geometric configurations from different methods, including HSE06, GGA-PBE, and LDA-PZ functionals.

ML structures. Figure 2f shows the binding energy versus the stacking pattern curve, where all the fifteen configurations have negative binding energy, indicating systems' exothermic feasibility. The binding energies for dynamically stable WSSe AAA, WSSe AA′A, and WSeTe AA′A structures are −188.560, −314.681, and −540.290 meV, respectively. Figure 2f reveals that, although configurations are homostructures for a particular material, binding energy varies for different stacking patterns. This variation in binding energy can be realized from different vdWs interactions due to the dissimilar atomic orientation of stacking patterns. As per atomic orientation dependence, stacking patterns AA′A and ABA have chalcogenide atoms of two layers are in line with the W atom of the other layer, unlike AAA, AB′A, and A′BA′ patterns (as shown in Figure 1). Thus, stacking patterns AA′A and ABA have comparable vdWs interactions and show higher negative binding energy than AAA, AB′A, and A′BA′ stacking patterns.

**3.2. Electronic Properties.** In Figure 3a−c, the band gap energies are depicted for all the five stacking patterns of WSSe, WSTe, and WSeTe materials using GGA-PBE, HSE06, and LDA-PZ functionals. This figure compares the band gap energies of dynamically stable structures WSSe AAA, WSSe AA′A, and WSeTe AA′A with the rest twelve structures using GGA-PBE, HSE06, and LDA-PZ functionals. To illustrate Figure 3, the individual band structure of each stacking pattern is drawn using the mentioned functionals as shown in Figures S1-S3 and listed in Table S1a−c. Our calculated band gap value for ML WSSe (the band structure is shown in Figure S1a using the HSE06 functional) is 2.07 eV, which is in correspondence with the previous reports.[36,37] Computed band gap values using the HSE06 functional for dynamically stable WSSe AAA, WSSe AA′A, and WSeTe AA′A structures are 1.63, 1.54, and 0.17 eV, respectively. Here, variation in the band gap of a particular WXY for different stacking patterns is because of the difference in vdWs interactions for the


https://doi.org/10.1021/acsomega.2c00244
ACS Omega 2022, 7, 12947−12955

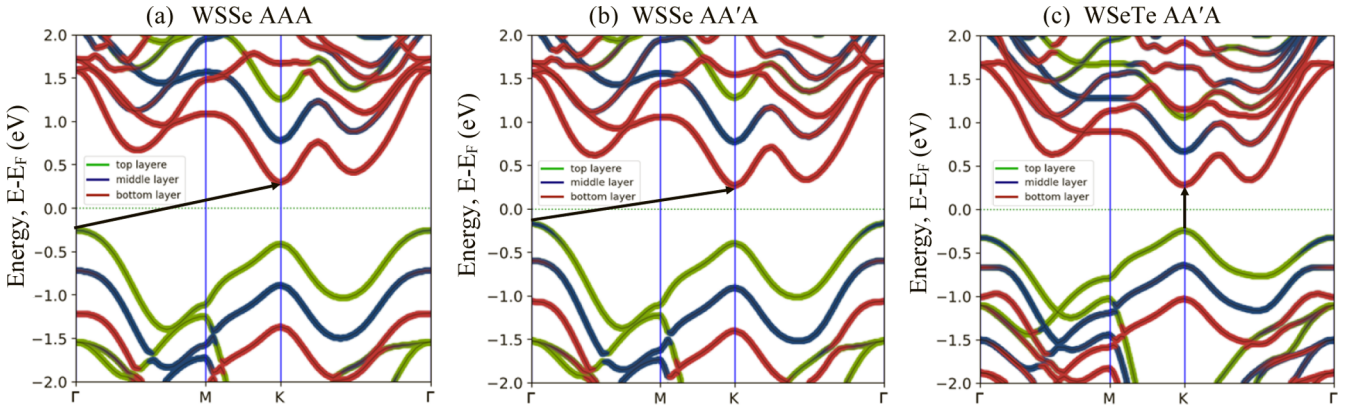


**Figure 4.** Layer-dependent band structure (LDA-PZ double zeta polarized LCAO basis set) for the trilayer homostructure of (a) WSSe AAA, (b) WSSe AA′A, and (c) WSeTe AA′A, and the color red, blue, and green lines represent the projections on the bottom, middle, and top layers, respectively.

dissimilar atomic orientations of stacking patterns. Because AA′A and ABA sacking patterns of a WXY have a comparable atomic orientation (chalcogenide atoms of two layers are in line with the W atom of the other layer), their band gap values are slightly different (Figure 3 and Table S1a−c). The band gap is found indirect and direct for all the stacking patterns of trilayer WSSe and trilayer WSeTe, respectively. Although the stacking patterns of trilayer WSeTe show a direct band gap, these configurations have a low band gap energy of ∼0.20 eV. Also, among the five stacking patterns of trilayer WSTe material, AAA, ABA, AB′A, and A′BA′ have indirect band gaps with a low band gap energy of ∼0.10 eV using the HSE06 functional, and the AA′A stacking pattern has a metallic band gap.

By stacking multiple WXY layers, the dipoles of the distinct layers are stacked, and an abrupt thin pn-junction can be found across the multilayer structure.[18] This presence of inherent polarization causes phenomena such as type-II band alignment. Type-II band alignment in a multilayer structure refers to the CB minimum (CBM) and VB maximum (VBM) being from different layers. To demonstrate this phenomenon on our dynamically stable WSSe AAA, WSSe AA′A, and WSeTe AA′A structures, layer projected band structures are illustrated in Figure 4 using the LDA-PZ functional. From Figure 4a,b, for dynamically stable WSSe AAA and WSSe AA′A structures, the relative position of the CBM (at K-point) is at 0.289 and 0.258 eV, respectively, mainly contributed by the bottom layer (red), and the relative position of the VBM (at Γ-point) is at −0.257 and −0.174 eV, respectively, mainly contributed by the top layer (green). From Figure 4c, for dynamically stable structure WSeTe AA′A, the relative position of the CBM (at *K*-point) is at 0.267 eV, mainly contributed by the bottom layer (red), and the relative position of the VBM (at K-point) is at −0.249 eV, mainly contributed by the top layer (green). Therefore, WSSe AAA and WSSe AA′A structures have indirect band gaps with type-II band alignment, and the WSeTe AA′A structure has a direct band gap with type-II band alignment. Also, to confirm the contribution of layers to CBM and VBM, layer projected densities of states are shown in Figures S4-S6. The VBM belonging to the top layer acts more p-like, and CBM belonging to the bottom layer acts more n-like,[18−20] which could enable the photogenerated holes and electrons of a solar cell to settle in the top layer and the bottom layer, respectively. Thus, the presence of type-II band alignment can ensure effective spatial separation of photogenerated electron−hole pairs by lowering the recombination rate of photogenerated carriers. To assist this fact, the band offset values are evaluated from the position of the band edge in the band structure of WSSe AAA, WSSe, and WSeTe AA′A are listed in Table 2,

**Table 2. Band Offset Calculated Using LDA-PZ Double-Zeta Polarized LCAO Basis Set Where $\Delta E_{c(BL-ML)}$/$\Delta E_{v(BL-ML)}$ (eV): At K Point Band Offset Between the Bottom Layer and the Middle Layer for CBM/VBM and $\Delta E_{c(TL-ML)}$/$\Delta E_{v(TL-ML)}$ (eV): At K Point Band Offset Between the Top Layer and the Middle Layer for CBM/VBM**

| | WSSe AAA | WSSe AA′A | WSeTe AA′A |
|---|---|---|---|
| $\Delta E_{c(BL-ML)}$ (eV) | 0.473 | 0.501 | 0.385 |
| $\Delta E_{c(TL-ML)}$ (eV) | 0.477 | 0.510 | 0.394 |
| $\Delta E_{v(BL-ML)}$ (eV) | 0.475 | 0.488 | 0.383 |
| $\Delta E_{v(TL-ML)}$ (eV) | 0.476 | 0.511 | 0.399 |

which indicates significant values of the band offset (∼0.5 eV). These large values of band offsets suggest the presence of the nondeteriorating parallel dipole moment for stacking layers and can act as a driving force for separating photogenerated carriers,[22] thus confining electrons in the bottom layer and holes in the top layer, which can increase the solar cell's conversion efficiency.

For extensive insights, the atomic orbital projected density of states (PDOSs) is evaluated for dynamically stable WSSe AAA, WSSe AA′A, and WSeTe AA′A structures, as shown in Figure 5. Figure 5 indicates that band edge states of the WSSe AAA and WSSe AA′A configurations are mainly contributed by the d orbital electrons of the W atom, and for WSeTe AA′A configuration, these are p orbital electrons. As the dispersion of d electrons is larger than p electrons, d−d transitions in WSSe AAA and WSSe AA′A configurations will result in more significant absorption efficiency than the WSeTe AA′A configuration.

To evaluate the effect of the number of stacking layers on band gap, layer-dependent band gap energy is shown in Figure 6 for dynamically stable WSSe AAA, WSSe AA′A, and WSeTe AA′A structures. Figure 6 reveals that as we increase the number of stacking layers in the WSeTe AA′A structure, band gap reduces considerably with stacking layers, and for bilayer and trilayer structures, the band gaps are ∼0.5 and ∼0.2 eV, respectively. Therefore, we will exclude the WSeTe AA′A


https://doi.org/10.1021/acsomega.2c00244
ACS Omega 2022, 7, 12947−12955

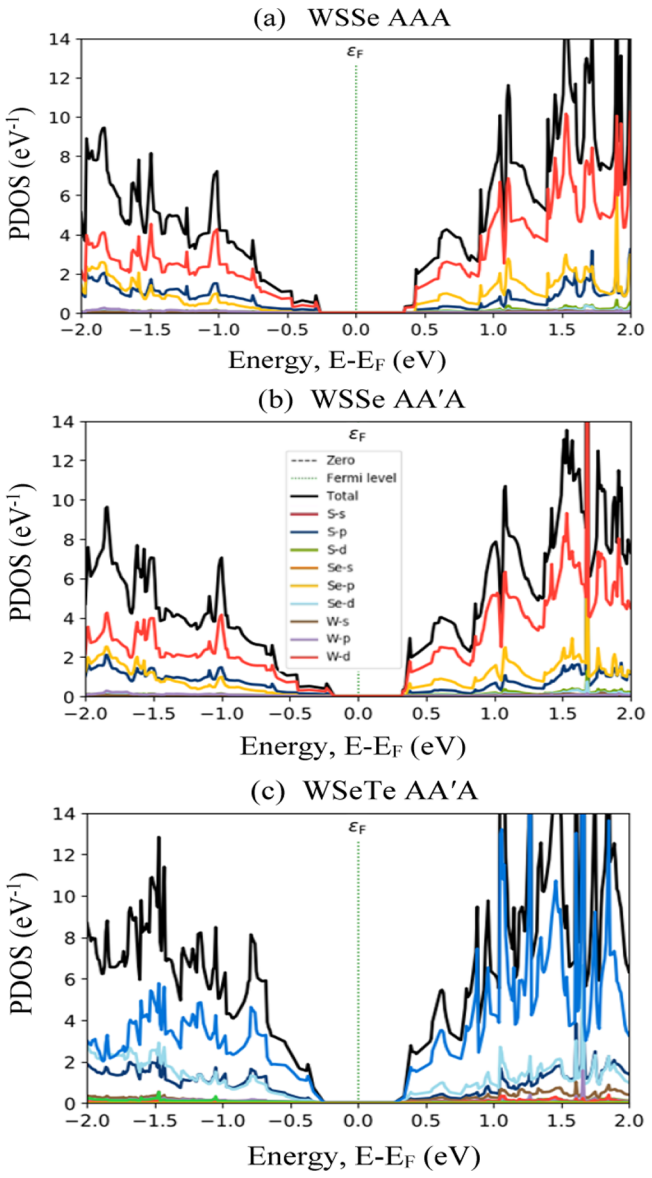


**Figure 5.** Atomic orbital PDOSs (LDA-PZ) for (a) WSSe AAA, (b) WSSe AA′A, and (c) WSeTe AA′A.

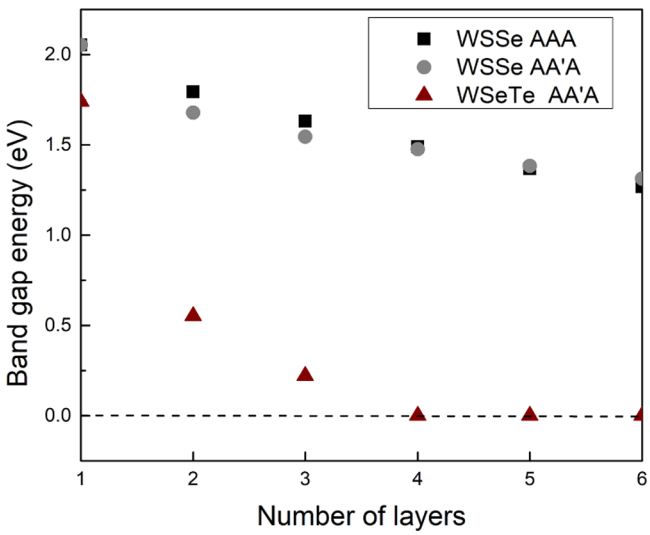


**Figure 6.** Number of layer-dependent band gap values for WSSe AAA, WSSe AA′A, and WSeTe AA′A using HSE06.

structure from our further optical property analysis. As for WSSe AAA and WSSe AA′A configurations, multilayer band gap values are compatible with the ML and relevant for efficient visible light absorption. Even though it is not convenient to increase the number of stacking layers to more than three because the possibility of tunneling transmission may be reduced due to the increase in distance between the top and bottom layers.

For further analysis, to get an inspection of the recombination time of separated photogenerated carriers in PV cells, carrier mobilities of WSSe AAA and WSSe AA′A configurations are calculated and listed in Table 3. Mobility calculations are evaluated from the carrier's effective mass, density, and conductivity using the dispersion band theory and the semi-classical BTE, where conductivity is expressed as a function of scattering and relaxation time. Both WSSe AAA and WSSe AA′A configurations show incredibly higher carrier mobility, indicating lower recombination time, and suggesting the potential of effective spatial carrier separation, signifying them as fascinating materials for PV technology.

**3.3. Optical Properties.** To get the consideration of the effectiveness of the WSSe AAA and WSSe AA′A configurations as a PV material, we have calculated core optical properties such as dielectric function, absorption coefficient, and reflectivity and made a comparison with the ML and bilayer with the same stacking pattern as shown in Figure 7a–d. The complex dielectric function as a function of photon energy is shown in Figure 7a,b to explain the dependence of optical properties of dynamically stable WSSe AAA and WSSe AA′A structures on the incident energy of light. Here, for the WSSe AAA and WSSe AA′A structures, the real part of the dielectric function has no negative portion within the energy range of 0–3.65 and 0–3.8 eV, respectively, instructing their semiconducting nature within these ranges. For both structures, the imaginary part of the dielectric functions shows a first peak similar to the ML and bilayer; thus, stacking three layers does not deteriorate the influence of the optical properties. The photon conversion efficiency of the proposed structures has been realized from the optical absorption coefficient values, as shown in Figure 7c. The significance of the dynamically stable trilayer WSSe AAA and WSSe AA′A homostructures over the ML and bilayer structures with similar stacking patterns can be comprehended from absorption coefficient values for the visible light range, as indicated in Figure 7c. For both proposed structures, these values can reach $3.5 \times 10^5$ $cm^{-1}$ (at ∼380 nm), comparable to the hybrid halide perovskites[38] and conventional optical absorber materials such as CdTe. As the number of stacking layers increased from single to trilayer, the absorption coefficient increased significantly, indicating higher photon conversion efficiency in trilayer than in mono- and bilayers. To proceed further, the reflectivity of dynamically stable WSSe AAA and WSSe AA′A structures are evaluated and shown in Figure 7d. The difference in atomic orientation between AAA and AA′A stacking patterns of the WSSe material results in the difference in reflectivity. The highest reflectivity for WSSe AAA is 16% (at 390 nm) for WSSe AA′A is 18% (at 390 nm) in the visible spectrum, suggestively low, signifying the low-loss nature of the materials. Furthermore, the energy differences between the band gap and direct band


https://doi.org/10.1021/acsomega.2c00244
ACS Omega 2022, 7, 12947–12955

Table 3. Electron Effective Mass, $m_e$*, Electron/Hole Density in *xy* Plan $n_e/n_h$ ($cm^{-2}$), Electron/Hole Conductivity $\sigma_e/\sigma_h$ (S/m), and Electron/Hole Mobility $\mu_e/\mu_h$ ($cm^2$/vs) at 300 K

| WXY | e effectivemass | h effectivemass | e density, $n_e$ 2d | h density, $n_h$ 2d | e conductivity, $\sigma_e$ | h conductivity, $\sigma_h$ | e mobility, $\mu_e$ | h mobility, $\mu_h$ |
|---|---|---|---|---|---|---|---|---|
| | ($m_e$*) | ($m_h$*) | ($cm^{-2}$) | ($cm^{-2}$) | (S/m) | (S/m) | ($cm^2$/vs) | ($cm^2$/vs) |
| WSSe AAA | 0.348 | 1.427 | $3.45 \times 10^0$ | $6.13 \times 10^2$ | $6.37 \times 10^{-6}$ | $9.93 \times 10^{-4}$ | $6.27 \times 10^4$ | $5.49 \times 10^4$ |
| WSSe AA′A | 0.349 | 0.891 | $2.38 \times 10^2$ | $4.47 \times 10^4$ | $3.94 \times 10^{-4}$ | $1.02e \times 10^{-1}$ | $5.34 \times 10^4$ | $7.38 \times 10^4$ |

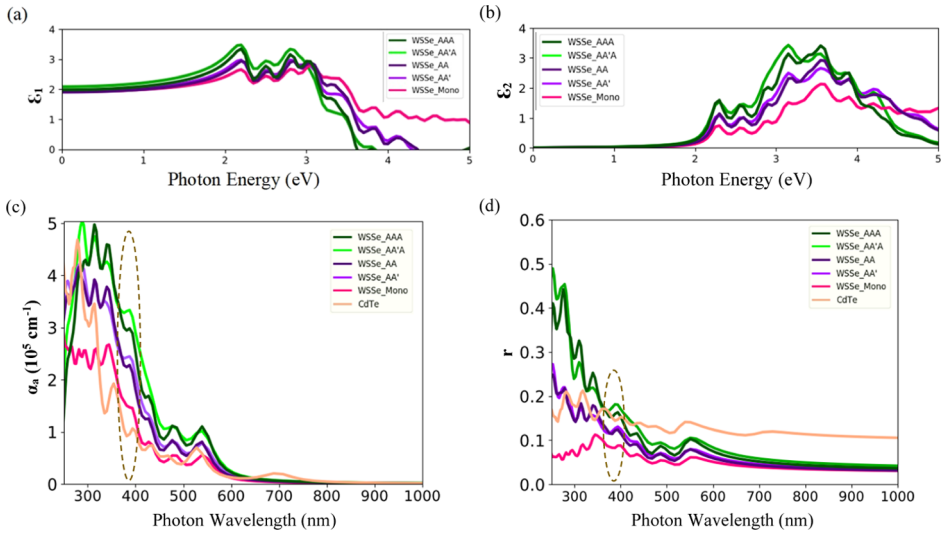


Figure 7. Comparison of photon energy-dependent (a) real dielectric function and (b) imaginary dielectric function and photon wavelength-dependent (c) absorption co-efficient and (d) reflectivity of WSSe AAA and WSSe AA′A with the ML and bilayer and cdTe.

gap ($E_g$-$k$) of the WSSe AAA and WSSe AA′A structures are 0.157 and 0.225 eV, respectively, from Table S1a, indicating their higher absorption efficiency. Thus, high-absorption efficiency and low reflectivity for the WSSe AAA and WSSe AA′A in the visible spectrum configurations indicate the PV competence of these materials, as well.

## 4. CONCLUSIONS

Using the first-principles DFT, the structural properties of Janus WXY (X ≠ Y = S, Se, and Te) trilayer homostructures for different stacking patterns have been analyzed. Electronic and optical properties are evaluated for the dynamically stable structures to analyze their appropriateness for fabricating PV devices. Because of having homogeneous staking layers, our proposed structures have an extremely low lattice mismatch (~0.05%). The trilayer WSSe AAA, WSSe AA′A, and WSeTe AA′A structures are found dynamically stable verified by phonon dispersion analysis. The WSeTe AA′A structure has the lowest binding energy and has a direct band gap of 0.221 eV. WSSe AAA and WSSe AA′A structures have indirect band gaps with suitable band gap values (1.63 and 1.55 eV, respectively) for absorbing photons at the visible light region with type-II band alignment, which signifies the possibility of spatial separation of photogenerated carriers with significant recombination time. The value of the electron mobility of the WSSe AAA (WSSe AA′A) structure is significantly high $6.27 \times 10^4$ $cm^2$ $v^{-1}$ $s^{-1}$ ($5.34 \times 10^4$ $cm^2$ $v^{-1}$ $s^{-1}$), and also the hole mobility is $5.49 \times 10^4$ $cm^2$ $v^{-1}$ $s^{-1}$ ($7.38 \times 10^4$ $cm^2$ $v^{-1}$ $s^{-1}$), and each of these structures has high band offsets values of ~0.5 eV. The optical absorption coefficients at visible spectrum $\sim 3.5 \times 10^5$ $cm^{-1}$ (at ~380 nm) are higher for the dynamically stable trilayer homostructures WSSe AAA and WSSe AA′A than their mono- and bilayer with similar stacking patterns. Thus, these results provide the basic understanding and guidance for the appropriateness of Janus WXY (X ≠ Y = S, Se, and Te) trilayer homostructures in PV devices.

## ■ ASSOCIATED CONTENT

### Supporting Information

The Supporting Information is available free of charge at https://pubs.acs.org/doi/10.1021/acsomega.2c00244.

Band structure using different functionals, PDOS, and lists of structural and electronic properties for different stacking patterns of Janus WXY (X ≠ Y = S, Se, and Te) trilayer homostructures and phonon dispersion curves for different stacking patterns of Janus WXY (X ≠ Y= S, Se, and Te) trilayer homostructures excluding WSSe AAA, WSSe AA′A, and WSeTe AA′A structures (PDF)

## ■ AUTHOR INFORMATION

### Corresponding Author

**Md. Tanvir Hasan** − *Department of Electrical and Electronic Engineering, Jashore University of Science and Technology (JUST), Jashore 7408, Bangladesh;* orcid.org/0000-0002-6304-3732; Email: tan_vir_bd@yahoo.com

### Authors

**Khadijatul Kubra** − *Department of Electrical and Electronic Engineering, Khulna University of Engineering & Technology (KUET), Khulna 9203, Bangladesh*

**Md. Rafiqul Islam** − *Department of Electrical and Electronic Engineering, Khulna University of Engineering & Technology (KUET), Khulna 9203, Bangladesh*

**Md. Sakib Hasan Khan** − *Department of Electrical and Electronic Engineering, Khulna University of Engineering & Technology (KUET), Khulna 9203, Bangladesh*



https://doi.org/10.1021/acsomega.2c00244
ACS Omega 2022, 7, 12947−12955

**Muhammad Shaffatul Islam** − *Department of Electrical and Electronic Engineering, World University of Bangladesh (WUB), Dhaka 1205, Bangladesh*

Complete contact information is available at: https://pubs.acs.org/10.1021/acsomega.2c00244

### Notes

The authors declare no competing financial interest.

The data generated and/or analyzed during the current study are not publicly available for legal/ethical reasons, but are available from the corresponding author upon reasonable request.

The research does not include human subjects, human data or tissue, or animals.

## REFERENCES

(1) Schuller, J. A.; Barnard, E. S.; Cai, W.; Jun, Y. C.; White, J. S.; Brongersma, M. L. Plasmonics for extreme light concentration and manipulation. *Nat. Mater.* **2010**, *9*, 193−204.

(2) Mounet, N.; Gibertini, M.; Schwaller, P.; Campi, D.; Merkys, A.; Marrazzo, A.; Sohier, T.; Castelli, I. E.; Cepellotti, A.; Pizzi, G.; Marzari, N. Two-dimensional materials from high-throughput computational exfoliation of experimentally known compounds. *Nat. Nanotechnol.* **2018**, *13*, 246−252.

(3) Miró, P.; Audiffreda, M.; Heine, T. An atlas of two-dimensional materials. *Chem. Soc. Rev.* **2014**, *43*, 6537−6554.

(4) Kang, J.; Liu, W.; Sarkar, D.; Jena, D.; Banerjee, K. Computational Study of Metal Contacts to Monolayer Transition-Metal Dichalcogenide Semiconductors. *Phys. Rev. X* **2014**, *4*, 031005.

(5) Luo, W.-M.; Shao, Z.-G.; Yang, M. Photogalvanic Effect in Nitrogen-Doped Monolayer MoS2 from First Principles. *Nanoscale Res. Lett.* **2019**, *14*, 380.

(6) Chaves, A.; Azadani, J. G.; Alsalman, H.; et al. Bandgap engineering of two-dimensional semiconductor materials. *npj 2D Mater. Appl.* **2020**, *4*, 29.

(7) Yu, X.; Sivula, K. Toward Large-Area Solar Energy Conversion with Semiconducting 2D Transition Metal Dichalcogenides. *ACS Energy Lett.* **2016**, *1*, 315−322.

(8) Yin, X.; Tang, C. S.; Zheng, Y.; Gao, J.; Wu, J.; Zhang, H.; Chhowalla, M.; Chen, W.; Wee, A. T. S. Recent developments in 2D transition metal dichalcogenides: phase transition and applications of the (quasi-)metallic phases. *Chem. Soc. Rev.* **2021**, *50*, 10087−10115.

(9) Wang, L.; Huang, L.; Tan, W. C.; Feng, X.; Chen, L.; Huang, X.; Ang, K.-W. 2D Photovoltaic Devices: Progress and Prospects. *Small Methods* **2018**, *2*, 1700294.

(10) Zhang, J.; Jia, S.; Kholmanov, I.; Dong, L.; Er, D.; Chen, W.; Guo, H.; Jin, Z.; Shenoy, V. B.; Shi, L.; Lou, J. Janus Monolayer Transition-Metal Dichalcogenides. *ACS Nano* **2017**, *11*, 8192−8198.

(11) Lin, Y.-C.; Liu, C.; Yu, Y.; Zarkadoula, E.; Yoon, M.; Puretzky, A. A.; Liang, L.; Kong, X.; Gu, Y.; Strasser, A.; Meyer, H. M.; Lorenz, M.; Chisholm, M. F.; Ivanov, I. N.; Rouleau, C. M.; Duscher, G.; Xiao, K.; Geohegan, D. B. Low Energy Implantation into Transition-Metal Dichalcogenide Monolayers to Form Janus Structures. *ACS Nano* **2020**, *14*, 3896−3906.

(12) Lu, A.-Y.; Zhu, H.; Xiao, J.; Chuu, C.-P.; Han, Y.; Chiu, M.-H.; Cheng, C.-C.; Yang, C.-W.; Wei, K.-H.; Yang, Y.; Wang, Y.; Sokaras, D.; Nordlund, D.; Yang, P.; Muller, D. A.; Chou, M.-Y.; Zhang, X.; Li, L.-J. Janus Monolayers of Transition Metal Dichalcogenides. *Nat. Nanotechnol.* **2017**, *12*, 744−749.

(13) Mak, K. F.; Shan, J. Photonics and optoelectronics of 2D semiconductor transition metal dichalcogenides. *Nat. Photonics* **2016**, *10*, 216−226.

(14) Li, F.; Wei, W.; Zhao, P.; Huang, B.; Dai, Y. Electronic and Optical Properties of Pristine and Vertical and Lateral Heterostructures of Janus MoSSe and WSSe. *J. Phys. Chem. Lett.* **2017**, *8*, 5959−5965.

(15) Wen, Y.-N.; Xia, M.-G.; Zhang, S.-L. Bandgap engineering of Janus MoSSe monolayer implemented by Se vacancy. *Comb. Mater. Sci.* **2018**, *152*, 20−27.

(16) Ju, L.; Bie, M.; Tang, X.; Shang, J.; Kou, L. Janus WSSe Monolayer: An Excellent Photocatalyst for Overall Water Splitting. *ACS Appl. Mater. Interfaces* **2020**, *12*, 29335−29343.

(17) Liu, X.; Gao, P.; Hu, W.; Yang, J. Photogenerated-Carrier Separation and Transfer in Two-Dimensional Janus Transition Metal Dichalcogenides and Graphene van der Waals Sandwich Heterojunction Photovoltaic Cells. *J. Phys. Chem. Lett.* **2020**, *11*, 4070−4079.

(18) Riis-Jensen, A. C.; Pandey, M.; Thygesen, K. S. Efficient Charge Separation in 2D Janus van der Waals Structures with Built-in Electric Fields and Intrinsic p-n Doping. *J. Phys. Chem. C* **2018**, *122*, 24520−24526.

(19) Palsgaard, M.; Markussen, T.; Gunst, T.; Brandbyge, M.; Stokbro, K. Efficient First-Principles Calculation of Phonon-Assisted Photocurrent in Large-Scale Solar-Cell Devices. *Phys. Rev. Appl.* **2018**, *10*, 014026.

(20) Palsgaard, M.; Gunst, T.; Markussen, T.; Thygesen, K. S.; Brandbyge, M. Stacked Janus Device Concepts: Abrupt pn-Junctions and Cross-Plane Channels. *Nano Lett.* **2018**, *18*, 7275−7281.

(21) Zhang, J.; Grzybowski, B. A.; Granick, S. Janus Particle Synthesis, Assembly, and Application. *Langmuir* **2017**, *33*, 6964−6977.

(22) Liu, H.; Huang, Z.; Wu, P.; Xue, W.; He, C.; Qi, X.; Zhong, J. Band offsets engineering in asymmetric Janus bilayer transition-metal dichalcogenides. *J. Phys.: Condens. Matter* **2020**, *32*, 035502.

(23) Yu, S.; Wei, W.; Li, F.; Huang, B.; Dai, Y. Electronic properties of Janus MXY/graphene (M = Mo, W; X ≠ Y = S, Se) van der Waals structures: a first-principles study. *Phys. Chem. Chem. Phys.* **2020**, *22*, 25675−25684.

(24) Wang, J.; Shu, H.; Zhao, T.; Liang, P.; Wang, N.; Cao, D.; Chen, X. Intriguing electronic and optical properties of two-dimensional Janus transition metal dichalcogenides. *Phys. Chem. Chem. Phys.* **2018**, *20*, 18571−18578.

(25) Clark, S. J.; Segall, M. D.; Pickard, C. J.; Hasnip, P. J.; Probert, M. I. J.; Refson, K.; Payne, M. C. First principles methods using CASTEP. *Z. Kristallogr.* **2005**, *220*, 567−570.

(26) Brandbyge, M.; Mozos, J.-L.; Ordejón, P.; Taylor, J.; Stokbro, K. Density-functional method for nonequilibrium electron transport. *Phys. Rev. B: Condens. Matter Mater. Phys.* **2002**, *65*, 165401.

(27) Perdew, J. P.; Burke, K.; Ernzerhof, M. Generalized Gradient Approximation Made Simple. *Phys. Rev. Lett.* **1996**, *77*, 2865−3868.

(28) Segall, M. D.; Lindan, P. J. D.; Probert, M. J.; Pickard, C. J.; Hasnip, P. J.; Clark, S. J.; Payne, M. C. First-principles simulation: ideas, illustrations and the CASTEP code. *J. Phys.: Condens. Matter* **2002**, *14*, 2717−2744.

(29) Koelling, D. D.; Harmon, B. N. A technique for relativistic spin-polarised calculations. *J. Phys. C: Solid State Phys.* **1977**, *10*, 3107.

(30) Grimme, S. Semiempirical hybrid density functional with perturbative second-order correlation. *J. Chem. Phys.* **2006**, *124*, 034108.

(31) Grimme, S. Accurate description of van der Waals complexes by density functional theory including empirical corrections. *J. Comput. Chem.* **2004**, *25*, 1463−1473.

(32) Gunst, T.; Markussen, T.; Stokbro, K.; Brandbyge, M. First-principles method for electron-phonon coupling and electron mobility: applications to two-dimensional materials. *Phys. Rev. B* **2016**, *93*, 035414.

(33) Giannozzi, P.; Baroni, S.; Bonini, N.; et al. QUANTUM ESPRESSO: a modular and open-source software project for quantum simulations of materials. *J. Phys.: Condens. Matter* **2009**, *21*, 395502.

(34) Khan, M. S. H.; Islam, M. S.; Islam, M. R.; Iskanderani, A.; Mehedi, I. M.; Hasan, M. T. Potential Visible-Light Driven PtO2/GaN vdW Hetero-Bilayer Photocatalysts for Water Splitting Using First-Principles. *IEEE Access* **2021**, *9*, 230−233.

(35) Gajdoš, M.; Hummer, K.; Kresse, G.; Furthmüller, J.; Bechstedt, F. Linear optical properties in the projector-augmented

wave methodology. *Phys. Rev. B: Condens. Matter Mater. Phys.* **2005**, *73*, 045112.
(36) Zhu, Z.; Ren, K.; Shu, H.; Cui, Z.; Huang, Z.; Yu, J.; Xu, Y. First-Principles Study of Electronic and Optical Properties of Two-Dimensional WSSe/BSe van der Waals Heterostructure with High Solar-to-Hydrogen Efficiency. *Catalysts* **2021**, *11*, 991.
(37) Lou, J.; Ren, K.; Huang, Z.; Huo, W.; Zhucand, Z.; Jin Yu, J. Electronic and optical properties of twodimensional heterostructures based on Janus XSSe (X= Mo, W) and Mg(OH)2: a first principles investigation. *RSC Adv.* **2021**, *11*, 29576.
(38) Kim, M. R.; Ma, D. Quantum-Dot-Based Solar Cells: Recent Advances, Strategies, and Challenges. *J. Phys. Chem. Lett.* **2015**, *6*, 85−99.



https://doi.org/10.1021/acsomega.2c00244
*ACS Omega* 2022, 7, 12947−12955